



1 **Characterization of aerosol hygroscopicity, mixing state, and**
2 **CCN activity at a suburban site in the central North China Plain**

3

4 Yuying Wang¹, Zhanqing Li¹, Yingjie Zhang², Wei Du^{2,3}, Fang Zhang¹, Haobo Tan⁴,
5 Hanbing Xu⁵, Xiaoi Jin¹, Xinxin Fan¹, Zipeng Dong¹, Qiuyan Wang⁶, Yele Sun^{2,3}

6

7

8 ¹College of Global Change and Earth System Science, Beijing Normal University, Beijing 100875,
9 China

10 ²State Key Laboratory of Atmospheric Boundary Layer Physics and Atmospheric Chemistry,
11 Institute of Atmospheric Physics, Chinese Academy of Sciences, Beijing 100029, China

12 ³College of Earth Sciences, University of Chinese Academy of Sciences, Beijing 100049, China

13 ⁴Key Laboratory of Regional Numerical Weather Prediction, Institute of Tropical and Marine
14 Meteorology, China Meteorological Administration, Guangzhou 510080, China

15 ⁵Shared Experimental Education Center, Sun Yat-sen University, Guangzhou 510275, China

16 ⁶Collaborative Innovation Center on Forecast and Evaluation of Meteorological Disasters, Nanjing
17 University of Information Science and Technology, Nanjing, 210044, China

18

19 *Correspondence to: Zhanqing Li (zli@atmos.umd.edu)

20

21



22 **Abstract.** Aerosol hygroscopicity, mixing state and CCN activity were investigated as
23 a part of the Atmosphere-Aerosol-Boundary Layer-Cloud (A²BC) Interaction Joint
24 Experiment carried out at Xingtai (XT), a suburban site in the center of the North
25 China Plain (NCP). In general, the probability density function of the hygroscopicity
26 parameter (κ -PDF) for 40–200 nm particles had a unimodal distribution and mean
27 κ -PDF patterns for different sizes were similar, suggesting that the particles were
28 highly aged and internally mixed because of strong photochemical reactions. The κ
29 calculated from the hygroscopic growth factor in the daytime and at nighttime showed
30 that photochemical reactions largely enhanced the aerosol hygroscopicity, and the
31 effect became weaker as the particle size increased. In addition, the aerosol
32 hygroscopicity was much larger at XT than at sites in the northern part of the NCP,
33 illustrating that the hygroscopicity of particles varies due to different emissions and
34 chemical processes in the NCP.

35 Measurement results also showed that new particle formation events occurred
36 frequently at XT, one of the most polluted city in China. The evolution of the
37 planetary boundary layer played a dominant role in aerosol mass concentration
38 changes while particle formation and growth had a greater influence on the variation
39 in aerosol number concentrations. Particle size was the most important factor
40 influencing the ability of aerosols to activate, especially at higher levels of
41 supersaturation (SS). The cloud condensation nuclei (CCN) number concentration
42 (N_{CCN}) derived from chemical composition was highly correlated with the measured
43 N_{CCN} ($R^2 \geq 0.85$), but was generally overestimated due to measurement uncertainties.



44 The effect of chemical composition on N_{CCN} was weaker relative to the particle size.
45 N_{CCN} sensitivity tests showed that the impact of chemical composition on N_{CCN}
46 became weaker with increasing SS, suggesting that chemical composition played a
47 less role in N_{CCN} estimations at higher SS levels. A good proxy for the chemical
48 comical composition ($\kappa = 0.31$) was found, which can simplify the calculation of
49 N_{CCN} on models.

50 **1. Introduction**

51 Aerosols, defined as the mixture of solid and liquid particles, are ubiquitously
52 present in the atmosphere because of direct emissions from biogenic and
53 anthropogenic sources and the secondary transformation from gas precursors. Aerosol
54 particles play an important role in climate changes through direct and indirect effects
55 (e.g. Ramanathan et al., 2001; Daniel et al., 2008; Z. Li et al., 2016). However, the
56 impact of aerosols on climate change is difficult to simulate because of the highly
57 variable physical and chemical properties of aerosols, and complex aerosol-cloud
58 interactions (IPCC, 2013; Lebo et al., 2017).

59 The hygroscopic growth and mixing state of aerosol particles are important for
60 estimating the direct climate effect of aerosols. This is because the growth and mixing
61 can change the particle size and optical properties of aerosol particles, directly
62 influencing the terrestrial radiation budget and degrading the atmospheric visibility
63 (Covert et al., 1972; Stock et al., 2011; Peng et al., 2016; Z. Li et al., 2017). In
64 addition, aerosol particles can be activated as cloud condensation nuclei (CCN) under



65 supersaturation (SS) conditions. The variability in CCN number concentration (N_{CCN})
66 can modify cloud microphysical properties, thereby causing an indirect radiative
67 forcing (Twomey, 1974; Albrecht, 1989). Previous studies have addressed three main
68 aerosol properties influencing the CCN activation, namely, particle size, chemical
69 composition, and mixing state. However, their relative importance is different in
70 different environments (e.g. Ervens et al., 2007; Cubison et al., 2008; Deng et al.,
71 2011; Zhang et al., 2014).

72 Ambient aerosols are composed of different species, including inorganic ions,
73 organic components, black carbon (BC), and mineral dust. Inorganics mainly contain
74 sulfate, nitrate, and ammonium, while organic aerosols (OA) consist of thousands of
75 chemicals (Jacobson et al., 2000). The hygroscopicity and CCN activity of a single
76 component can be characterized according to laboratory studies (e.g. Petters and
77 Kreidenweis, 2007), but the properties of their mixtures are hard to estimate because
78 of the different chemical species and mixing states of particles in the atmosphere.
79 Therefore, aerosol hygroscopicity and CCN activity are very different in different
80 regions. Comprehensive field measurements of aerosol properties in different areas
81 are necessary to improve models.

82 China, especially the North China Plain (NCP), has been suffered from severe air
83 pollution since its rapid industrialization and urbanization in the last couple of
84 decades, where diverse sources and aging processes make aerosol properties
85 particularly diverse and complex. As such, the region has drawn much attention in
86 studying the aerosol mixing state, hygroscopicity, and CCN activity (Deng et al., 2011;



87 Liu et al., 2011; Zhang et al., 2014; F. Zhang et al., 2016; S.L. Zhang et al., 2016; Wu
88 et al., 2016; Y. Wang et al., 2017). Liu et al. (2011) and Y. Wang et al. (2017) have
89 suggested that ambient particles are mostly an external mixture with different
90 hygroscopicities. Deng et al. (2011) has shown that the aerosol number size
91 distribution is critical in the prediction of N_{CCN} while Zhang et al. (2014) have
92 highlighted the importance of chemical composition in determining particle activation
93 properties. However, all these studies were done using data from the northern part of
94 the NCP. Few studies have focused on the central region of the NCP. Compared to the
95 northern part of the NCP, the central part of the NCP is more affected by industrial
96 emissions where a dense cluster of China's heavy industries exist (Fu et al., 2014).
97 Measurement of aerosol properties in the central part of the NCP are critically needed
98 to investigate the impact of air pollution on the environment and climate changes.

99 Xingtai (XT), a city located in the middle of the NCP, often ranks in the top of
100 polluted cities in China. Local industrial and domestic sources are the greatest
101 contributors to severe haze events (Wang et al., 2014). A field experiment called the
102 Atmosphere-Aerosol-Boundary Layer-Cloud (A^2BC) Interaction Joint Experiment
103 was carried out at a suburban site in Xingtai in the summer of 2016. Differences in
104 aerosol properties at this site and at sites in the northern part of the NCP were found in
105 this study.

106 The paper is organized as follows. Sections 2 and 3 describe the measurement
107 method and data analysis theory. Section 4 presents and discusses the measurement
108 results, which includes the data time series, aerosol mixing state, hygroscopicity, CCN



109 prediction and its sensitivity to chemical composition. A summary and conclusions are
110 given in section 5.

111 **2. Measurements**

112 **2.1. Sampling site and meteorology**

113 The A²BC was carried out at the national weather station located in XT (37.18°N,
114 114.36°E) from 1 May to 15 June of 2016. This site is situated in southern Hebei
115 Province, located in the central part of the NCP and to the east of Taihang Mountains
116 (Fig. 1a). This region is heavily populated, urbanized, and industrialized. The major
117 industrial manufacturers include coal-based power plants, steel and iron works,
118 glassworks, and cement mills. The weak diffusion conditions and heavy industrial
119 emissions lead to exceptionally high concentrations of particulate matter (PM) with
120 diameter less than 10 μm (PM₁₀) and 2.5 μm (PM_{2.5}), as well as gas pollutants such as
121 sulfur dioxide (SO₂), and nitrogen oxides (NO_x) during the frequent occurring haze
122 episodes in this region (Wang et al., 2014; Fu et al., 2014). Figure 1b shows the mean
123 distribution of SO₂ concentrations from May of 2012 to 2016, confirming that the
124 measurement site is located in the pollution center of this region.

125 Time series of meteorological variables measured at the weather station are
126 shown in Fig. S1. This site is heavily affected by the mountain-valley wind, showing a
127 prevailing southeasterly wind during the day and a northwesterly wind at night (Fig.
128 S1 and Fig. S2). There was almost no precipitation during the study period. The
129 ambient temperature (*T*) and relative humidity (RH) time series show opposing trends.



130 Campaign-mean values of T and RH are 21.9 °C and 51.6 %, respectively.

131 **2.2. Instrumentation and operation**

132 **2.2.1. Aerosol hygroscopicity measurements**

133 The hygroscopicity tandem differential mobility analyzer (H-TDMA) used in this
134 study has been described in detail by others (Tan et al., 2013; Y. Wang et al., 2017).
135 Briefly, ambient aerosols are first dried and neutralized by a Nafion dryer and a soft
136 X-ray charger. A differential mobility analyzer (DMA₁, model 3081L, TSI Inc.) is
137 used to select monodispersed particles of a certain diameter (D_{p0}). The monodispersed
138 particles are then passed through a Nafion humidifier with a controlled higher RH and
139 are humidified. A second DMA (DMA₂, same model as the DMA₁) and a water-based
140 condensation particle counter (WCPC, model 3787, TSI Inc.) are used to measure the
141 number size distribution of the humidified particles. The DMA₁ and WCPC can also
142 be connected directly to measure the 10–400 nm particle number size distribution
143 (PNSD). In this study, the dry diameters selected by the DMA₁ are 40, 80, 110, 150,
144 and 200 nm. The humidified RH is set to 85 %.

145 The hygroscopic growth factor (GF) is defined as the ratio of the humidified
146 diameter at a given RH to the dry diameter:

$$147 \quad GF = \frac{D_p(\text{RH})}{D_{p0}}, \quad (1)$$

148 where $D_p(\text{RH})$ is the particle diameter at the given RH and D_{p0} is the dry diameter
149 selected by the DMA₁. The measured distribution function versus GF (GF-MDF) can
150 be calculated with WCPC data downstream from the DMA₁ and DMA₂. The GF



151 probability density function is then retrieved using the TDMAFIT algorithm
152 (Stolzenburg and McMurry, 1988, 2008).

153 **2.2.2. Aerosol chemical composition measurements**

154 The Aerosol Chemical Speciation Monitor (ACSM) was deployed to measure the
155 non-refractory submicron aerosol (NR-PM₁) species (sulfate, nitrate, ammonium,
156 chloride, and organics) in real-time. A PM_{2.5} URG cyclone (model URG-2000-30ED)
157 was installed in the front of the sampling inlet to remove coarse particles (> 2.5 μm in
158 diameter). Before sampling into the ACSM, aerosol particles were dried (below 40 %
159 RH) by a silica gel diffusion dryer. In addition, the ACSM was calibrated routinely
160 with pure ammonium nitrate to determine its ionization efficiency. More detailed
161 descriptions about the ACSM are given by Ng et al., (2011) and Sun et al., (2012). A
162 positive matrix factor analysis is used to analyze the organic spectral matrices
163 according to Ulbrich et al., (2009). Three factors, i.e., hydrocarbon-like OA (HOA),
164 cooking OA (COA), and oxygenated OA (OOA), are chosen as the ACSM dataset.
165 HOA and COA are both anthropogenic primary organic aerosols (POA) while OOA is
166 the secondary organic aerosol (SOA).

167 The ACSM does not detect refractory material such as BC, so a seven-wavelength
168 aethalometer (AE-33, Magee Scientific Corp.) was used to measure the BC mass
169 concentration of BC particles with diameters < 1.0 μm (BC PM₁). Mineral dust and
170 sea salt are the other refractory species, but they typically exist in the coarse mode and
171 make negligible contributions to PM₁ (Juranyi et al., 2010; Meng et al., 2014).



172 **2.2.3. Aerosol size distribution and CCN measurements**

173 The aerosol particle number size distribution (15–685 nm) was measured by a
174 scanning mobility particle sizer (SMPS) that was equipped with a long DMA (model
175 3081L, TSI Inc.) and a condensation particle counter (CPC, model 3775, TSI Inc.). A
176 single-column continuous-flow stream-wise thermal-gradient cloud condensation
177 nuclei counter (CCNC-100, DMT Inc.) was applied to measure the bulk CCN number
178 concentration. Five SS levels, i.e., 0.07, 0.1, 0.2, 0.4, and 0.8 %, were set in the
179 CCNC and the running time was 10 min for each SS level. The SS in the CCNC are
180 calibrated with pure ammonium sulfate (Rose et al., 2008) before and after the
181 measurement campaign. The corrected SS levels are 0.11, 0.13, 0.22, 0.40, and 0.75 %,
182 respectively.

183 The aerosol activation ratio (AR) at a certain SS is calculated as N_{CCN} divided by
184 the total particle number concentration in the 15–685 nm range ($N_{15-685 \text{ nm}}$), i.e., $\text{AR} =$
185 $N_{\text{CCN}} / N_{15-685 \text{ nm}}$. The particle number concentration below 15 nm is not measured by
186 the SMPS, but this does not affect the calculated N_{CCN} because the activation critical
187 diameter is always larger than 15 nm at these SS levels (Zhang et al., 2014). Aerosol
188 particles with diameters larger than 685 nm are also not detected by the SMPS. These
189 larger particles will always act as CCN due to their larger dry sizes. However, the
190 number concentration above 685 nm in the atmosphere is always negligible (Juranyi
191 et al., 2010).



192 **2.2.4. Other measurements**

193 In this study, a micro-pulse lidar (MPL-4B, Sigmaspace Corp.) was used to study
194 the evolution of the planetary boundary layer (PBL). The pulse repetition rate of the
195 MPL was 2.5 kHz at a visible wavelength of 532 nm. The peak value of the optical
196 energy of the laser beam was 8 μ J. The pulse duration ranged from 10 to 100 ns, and
197 the pulse interval was set to 200 ns, corresponding to a spatial resolution of 30 m. The
198 MPL-retrieved PBL height is the altitude where a sudden decrease in the scattering
199 coefficient occurs (Brooks, 2003; Quan et al., 2013).

200 Trace gas analyzers were used to measure the gaseous species of ozone (O_3) and
201 SO_2 . SO_2 was measured using an SO_2 analyzer with a fluorescence cell (Ecotech
202 model 9850A) and O_3 was measured using an O_3 analyzer (Ecotech model 9810B)
203 with ultraviolet absorption technology. More detailed descriptions about the trace gas
204 analyzers are given by Zhu et al., (2016).

205 **3. Theory**

206 **3.1. Hygroscopicity parameter**

207 To link hygroscopicity measurements below and above water vapor saturation,
208 the Köhler theory (Köhler, 1936) is parameterized using the hygroscopicity parameter
209 κ (Petters and Kreidenweis, 2007). This is known as the κ -Köhler theory. According
210 to the theory, the equilibrium equation over a solution droplet at a saturation ratio
211 $S(D)$ is



$$S(D) = \frac{D^3 - D_d^3}{D^3 - D_d^3(1 - \kappa)} \exp\left(\frac{4\sigma_{s/a}M_w}{RT\rho_w D}\right), \quad (2)$$

212 where D and D_d are the wet and dry droplet diameters, respectively, $\sigma_{s/a}$ is the
213 surface tension coefficient, M_w is the mole mass of water, R is the universal gas
214 constant, T is the temperature, and ρ_w is the density of water.

215 Below the water vapor saturation, $S(D)$ is RH, D is $D_p(\text{RH})$, and D_d is D_{p0}
216 in Eq. (1). The κ parameter is then calculated using H-TDMA data according to Eq. (1)
217 and Eq. (2):

$$\kappa_{\text{gf}} = (\text{GF}^3 - 1) \cdot \left[\frac{1}{\text{RH}} \exp\left(\frac{4\sigma_{s/a}M_w}{RT\rho_w D_d \text{GF}}\right) - 1 \right]. \quad (3)$$

218 For a multicomponent particle, the Zdanovskii–Stokes–Robinson (ZSR) mixing
219 rule (Stokes and Robinson, 1966) can also estimate κ using chemical composition
220 data:

$$\kappa_{\text{chem}} = \sum_i \varepsilon_i \kappa_i, \quad (4)$$

221 where ε_i and κ_i are the volume fraction and hygroscopicity parameter for the i th
222 chemical component. The ACSM provides the mass concentrations of inorganic ions
223 and organics. A simplified ion-pairing scheme such as that described by Gysel et al.,
224 (2007) was applied to convert ion mass concentrations to mass concentrations of their
225 corresponding inorganic salts (see Table S1 in the supplement). Table S1 also lists κ
226 and the gravimetric density of each individual component. In the following
227 discussions, κ_{gf} and κ_{chem} denote the hygroscopicity parameters derived from
228 H-TDMA measurements and estimated using the ZSR mixing rule, respectively.
229
230
231



232 3.2. CCN estimation

233 The critical supersaturation (s_c , $s_c = S_c - 1$) for a dry diameter (D_d) of a particle with
234 hygroscopicity κ is calculated from the maximum of the κ -Köhler curve (Eq. 1)
235 (Petters and Kreidenweis, 2007). The s_c - D_d relationship is then established. According
236 to this relationship, the critical diameter ($D_{0,crit}$) can be calculated using the estimated
237 κ_{chem} (Eq. 4) at the SS set in the CCNC. All particles larger than $D_{0,crit}$ will activate
238 as CCN, assuming that aerosols are internally mixed. Then the CCN number
239 concentration can be estimated from the integral of the aerosol size distribution
240 provided by the SMPS from $D_{0,crit}$ to the largest measured size.

241 4. Results and discussion

242 4.1. Overview

243 Figures 2 and 3 show the time series of the main aerosol properties during the
244 field experiment. The PNSD changes dramatically (Fig. 2a) and the aerosol number
245 concentration in the 15–50 nm range ($N_{15-50\text{ nm}}$) increases sharply in the morning
246 almost every day (Fig. 2b). The time series of the mean diameter (D_p) of particles also
247 shows that a growth process occurs after the sharp increase in $N_{15-50\text{ nm}}$. All these
248 phenomena suggest that new particle formation (NPF) events occurred frequently at
249 XT during the field experiment (Kulmala et al., 2012; Y. Li et al., 2017). This is likely
250 related to the high concentration of gas precursors mainly from local emissions. High
251 emissions of SO_2 and volatile organic compounds associated with the high oxidation



252 capacity in a polluted atmosphere make NPF events occur more frequently in north
253 China (Z. Wang et al., 2017).

254 Figure 2c-d shows the time series of the probability density function of κ_{gf}
255 (κ -PDF) for 40 nm and 150 nm particles, respectively. In general, mono-modal
256 κ -PDFs are observed. This is different from κ -PDFs at other sites in China where bi-
257 and tri-modal distributions are dominant (Liu et al., 2011; Ye et al., 2013; Jiang et al.,
258 2016; S.L. Zhang et al., 2016; Y. Wang et al., 2017). This is due to differences in the
259 aerosol mixing state, which will be discussed in section 4.2.

260 The bulk mass concentrations of organics, sulfate, nitrate, ammonium, and
261 chloride measured by the ACSM are shown in Fig. 3a, along with the BC mass
262 concentration measured with the AE-33. Organics and sulfate are the dominant
263 chemical species with mass fractions in PM_{10} of 39.1 % and 24.7 %, respectively.
264 Figure 3b-c shows the volume fractions of paired chemical compositions and the
265 hygroscopicity parameter derived from κ_{chem} , respectively. The average volume
266 fraction of inorganics ($(NH_4)_2SO_4+NH_4HSO_4+H_2SO_4+NH_4NO_3$) is similar to that of
267 organics (POA+SOA), but their volume fractions change diurnally. The volume
268 fraction of inorganics increases during daytime while the volume fraction of organics
269 decreases. In addition, SOA is the dominant contributor to OA, accounting for ~69 %
270 of the organics volume. This shows that photochemical reactions were strong at XT
271 during the field experiment (Huang et al., 2014). The mean κ_{chem} in Fig. 3c is 0.31
272 with values ranging from 0.20 to 0.40. The trend in κ_{chem} is similar to that of the
273 volume fraction of inorganics, suggesting that inorganics played a key role when it



274 comes to κ_{chem} (Wu et al., 2016).

275 **4.2. Aerosol mixing state and hygroscopicity**

276 The average probability density functions of κ_{gf} (κ -PDF) for different particle
277 sizes derived from H-TDMA data are shown in Fig. 4. For all particle sizes considered,
278 κ_{gf} ranges from 0 to 0.8 and the κ -PDF patterns are similar, suggesting that the
279 hygroscopic compounds in different particle size mode were similar at XT during the
280 field experiment. In general, κ -PDF patterns show only one hydrophilic mode with
281 weak hydrophobic modes occasionally appearing at night when photochemical
282 reactions are weak (Fig. S3). This is different from what has been reported at other
283 sites in China (Liu et al., 2011; Ye et al., 2013; Jiang et al., 2016; Zhang et al., 2016;
284 Y. Wang et al., 2017) where the κ -PDF patterns always show bi- or tri-modal
285 distributions. Based on previous studies (Liu et al., 2011; Y. Wang et al., 2017),
286 ambient aerosols can be classified into three groups according to their κ_{gf} values:

287 — nearly hydrophobic (NH): $\kappa_{\text{gf}} < 0.1$

288 — less hygroscopic (LH): $0.1 \leq \kappa_{\text{gf}} < 0.2$

289 — more hygroscopic (MH): $0.2 \leq \kappa_{\text{gf}}$

290 Table 1 gives the number fractions of each group for different particle sizes. The MH
291 group dominates all particle sizes. The number fractions of the NH and LH groups are
292 less than 6.0 % each. However, the volume fractions of hydrophobic BC and
293 low-hygroscopic organics (where κ_{BC} is approximately zero and κ_{organic} is
294 typically less than 0.1) are ~10.1 % and 47.4 % according to chemical composition



295 measurements (Fig. 3b). This suggests that the particles were highly aged and
296 internally mixed at XT during the field experiment. Coating of sulfates and secondary
297 organics during the aging process changes the structure of BC and makes it grow,
298 which can significantly enhance the hygroscopicity of particles (e.g., Zhang et al.,
299 2008; Jimenez et al., 2009; Tritscher et al., 2011; Guo et al., 2016). In addition, the
300 observed unimodal distribution of κ -PDF also suggests the highly internally mixed
301 state of the particles (Swietlicki et al., 2008).

302 Figure 5 shows the average size-resolved κ_{gf} derived from H-TDMA data at XT
303 and at other sites in China. At XT, κ_{gf} for different particle sizes are larger in the
304 daytime than at night and the difference between daytime and nighttime decreases
305 with increasing particle size. This suggests that the impact of photochemical reactions
306 on aerosol hygroscopicity was strong and that the effect was weaker with increasing
307 particle size.

308 The magnitude of κ_{gf} is larger at XT than at other sites of China. In particular,
309 the magnitude of κ_{gf} is much larger at XT than at sites in the northern part of the
310 NCP, i.e., Beijing, Wuqing, and Xianghe. The lower κ_{gf} in the urban area of Beijing
311 is likely related to the more severe traffic emissions (Ye et al., 2013; Wu et al., 2016).
312 Wuqing and Xianghe are located in the suburban area between the two megacities of
313 Beijing and Tianjin and are simultaneously affected by traffic and industrial emissions.
314 The magnitude of κ_{gf} at these two sites are higher than at Beijing but lower than at
315 XT. Although XT is located far away from these megacities, it is situated in the
316 industrial center of the NCP, so the higher concentrations of precursors and strong



317 photo chemical reactions make the particles more internally mixed and highly aged.
318 This is why κ_{gf} in XT is larger than at other sites. This suggests that the
319 hygroscopicity of particles from different emissions and chemical processes differ in
320 NCP. In addition, 40 nm particles are always more hygroscopic than 80 nm particles
321 at XT, especially in the daytime, which is also different from other sites. This is likely
322 because the coating effect of sulfates and secondary organics is more significant on
323 smaller particles (Tritscher et al., 2011; Guo et al., 2016). Furthermore, since the field
324 measurements took place in a local with heavy industrial activities, it is possible that
325 amine contributes significantly to the hygroscopicity of 40 nm particles. Several
326 studies have shown that amine compounds in aerosol phase can be hygroscopic,
327 sometimes at even low RH (e.g. Qiu and Zhang, 2012; Chu et al., 2015;
328 Gomez-Hernandez et al., 2016).

329 **4.3. Diurnal variations in aerosol properties**

330 **4.3.1. Diurnal variations in aerosol number and mass concentrations**

331 Figure 6a shows the diurnal variation in MPL-derived PBL height. PBL height
332 can be determined at the altitude where a sudden decrease in the scattering coefficient
333 occurs from the MPL data (Cohn and Angevine, 2000; Brooks, 2003). Note that the
334 retrieved PBL height is only valid from 07:00 local time (LT) to 19:00 LT (Quan et al.,
335 2013). The retrieved PBL height at night is not accurate because of the likely
336 influence of residual aerosols within the nocturnal PBL. The evolution of PBL height
337 from 07:00 LT to 19:00 LT is sufficient to analyze its link with the change in aerosol



338 number and mass concentrations during the daytime. Figure 6b shows diurnal
339 variations in aerosol number and mass concentrations in the 15–685 nm range (N_{15-685}
340 nm and PM_{15-685} nm, respectively). Variations in the N_{15-685} nm and PM_{15-685} nm trends
341 oppose each other. From 08:00 LT to 14:00 LT, the PBL height lifts from ~0.5 km to
342 ~0.6 km, while PM_{15-685} nm decreases from ~24 $\mu\text{g m}^{-3}$ to ~19 $\mu\text{g m}^{-3}$ although there is
343 a slight increase at the beginning of the period. This suggests the important effect of
344 PBL evolution on PM_{15-685} nm. However, N_{15-685} nm sharply increases from ~7600 cm^{-3}
345 at 07:00 LT to ~13000 cm^{-3} at 13:00 LT. This is related to the sudden burst of
346 nucleation mode particles (< 100 nm) when NPF events occurred. Newly formed fine
347 particles contribute little to PM_{15-685} nm. In the evening, PM_{15-685} nm increases
348 gradually while N_{15-685} nm decreases. This is attributed to the declining trend in the
349 nocturnal PBL and particle coagulation and growth. In other words, the evolution of
350 the PBL plays a dominant role on the aerosol mass concentration, while particle
351 formation and growth has a greater influence on the variation in aerosol number
352 concentration.

353 4.3.2. Diurnal variation in aerosol hygroscopicity

354 Figure 6c shows diurnal variations in κ_{gf} and κ_{chem} . All sized κ_{gf} increases
355 beginning from the NPF event, especially for the 40 nm particles. The increase of κ_{gf}
356 in the morning was synchronous with the particle number concentration (N_{15-685} nm)
357 but not with the PBL height, further suggesting the impact of photochemical reactions
358 on aerosol hygroscopicity. The κ_{gf} for 40 nm particles increases from ~0.32 at 07:00



359 LT to ~ 0.44 at 15:00 LT, and approaches the κ of pure ammonium sulfate
360 [$\kappa_{\text{gf},(\text{NH}_4)_2\text{SO}_4} = 0.48$ (Wu et al., 2016)]. This suggests that a large amount of sulfates
361 were produced through the photochemical reactions of precursors. This can be verified
362 from the diurnal variation in chemical composition (Fig. 6d), which shows that the
363 mass fraction of sulfate increased during the daytime while the mass fraction of
364 organics (POA or SOA) varied more weakly. The diurnal variation in SO_2 precursor
365 also shows this (Fig. S4). The diurnal variation in κ_{gf} for 80–200 nm particles differs
366 from that of 40 nm particles. The differences in κ_{gf} between 80–200 nm particles in
367 the early morning are large but gradually decrease as the sun rises. After 11:00 LT, the
368 κ_{gf} for 80–200 nm particles are similar but lower than that of 40 nm particles,
369 suggesting that the enhanced hygroscopicity in the 80–200 nm particles was likely
370 caused by the condensation of sulfates and secondary organics while that of the 40 nm
371 particles was caused by the growth of the new particles.

372 Figure 6c also shows that the κ_{chem} for PM_{10} is lower than the κ_{gf} for 40–200
373 nm particles and has a weaker diurnal variation. Two reasons may explain this: (1) the
374 bulk chemical compositions of PM_{10} and of 40–200 nm particles differ greatly and (2)
375 the ZSR model cannot describe the impact of condensation on aerosol hygroscopicity
376 very well. During the daytime, the condensation of sulfuric acid on organics or BC
377 greatly enhances their hygroscopicity (Zhang et al., 2008; Zhang et al., 2009). Cruz
378 and Pandis (2000) have shown that the measured κ_{gf} of internally mixed
379 $(\text{NH}_4)_2\text{SO}_4$ -organic aerosols is larger than the predicted κ_{chem} based on the ZSR
380 model.



381 In summary, the ample supply of effluent SO₂ and VOCs provided sufficient
382 precursors for the strong photochemical reactions at XT during the field experiment,
383 and the produced sulfates and the condensation of sulfuric acid enhanced aerosol
384 hygroscopicity, especially during the day. This also suggests that the observed
385 frequent NPF events were mainly induced by the oxidation of precursors.

386 **4.3.3. Diurnal variation in CCN number concentration and activation ratio**

387 Figure 7a shows the diurnal variations in N_{CCN} and AR at different SS. In the
388 morning, N_{CCN} first decreases then increases while AR shows the opposite trend. This
389 is related to the evolution of the PBL and NPF events. At the initial stage of an NPF
390 event, the newly formed particles are less than 15 nm in size, which is below the
391 detection limit of the SMPS. As a result, $N_{15-685\text{ nm}}$ decreases (Fig. 6b) as the PBL lifts
392 and N_{CCN} also decreases. However, the mixing of aged particles within the PBL makes
393 the particle size (Fig. 7b) and AR increase slightly. With condensation and the growth
394 of new particles, fine particles detected by the SMPS increase rapidly but a portion of
395 them cannot be activated because their smaller size. So N_{CCN} increases but AR
396 decreases from 08:00 LT to 14:00 LT. In the afternoon and evening, N_{CCN} and AR
397 increase slightly with the increase in particle size (Fig. 7b). However, these trends
398 become weaker as SS decreases, likely because the critical diameter is larger at low
399 SS and the influence of aerosol size distribution on N_{CCN} and AR is relatively weaker.
400 This demonstrates that the particle size is the most important factor influencing the
401 aerosol activation ability and the CCN number concentration, especially at larger SS



402 levels.

403 **4.4. CCN estimation from chemical composition data**

404 The three main factors influencing CCN activation are particle size, mixing state,
405 and chemical composition. As discussed in the above sections, particles are highly
406 internally mixed at XT and particle size has a great influence on N_{CCN} . In this section,
407 a CCN closure study is conducted and the impact of chemical composition on N_{CCN} is
408 discussed. Figure 8a shows estimated N_{CCN} as a function of measured N_{CCN} using
409 real-time κ_{chem} . The estimated N_{CCN} correlates well with measurements ($R^2 \geq 0.85$)
410 but is generally overestimated. The slope of each linearly fitted line is greater than
411 1.10 and increases with increasing SS. In addition, the relative deviation (RD)
412 increases from 16.2 % to 25.2 % as SS increases from 0.13 % to 0.75 %, suggesting
413 that estimates become worse at larger SS. The overestimation of N_{CCN} is mainly
414 caused by large measurement uncertainties of CCNC: (1) the temperature or high flow
415 rates in the CCNC may not allow enough time for particles to reach sizes large
416 enough to be counted by the OPC at the exit of the CCN chamber (Lance et al., 2006;
417 Cubison et al., 2008) and (2) in high particle number concentration environments,
418 water depletion in the CCNC may reduce the counting rate of the CCNC (Deng et al.,
419 2011). These uncertainties make measured N_{CCN} lower than the actual N_{CCN} . At larger
420 SS, those activated aerosols in the cloud chamber of CCNC are greater in number and
421 smaller in size, so the impact of these uncertainties is greater. Another discussion
422 about this problem can be found in the supplement (Fig. S5).



423 Figure 8b shows estimated N_{CCN} using the mean value for κ_{chem} ($\kappa_{chem} = 0.31$).
424 Compared with results using real-time values for κ_{chem} , the fit parameters and RD
425 change slightly, suggesting that the effect of chemical composition on N_{CCN} is weaker
426 relative to the particle size. The sensitivity of estimated N_{CCN} to the variability in
427 chemical composition (κ_{chem}) is further investigated (Fig. 9). In this figure, the
428 variability of the equipotential lines in RD suggests that the sensitivity of N_{CCN} is
429 strongly time dependent. This is attributed to the variability of the shape of the aerosol
430 size distribution (Juranyi et al., 2010). The sensitivity of N_{CCN} to chemical
431 composition (κ_{chem}) becomes weaker with increasing SS, suggesting that chemical
432 composition becomes less important in N_{CCN} estimates at larger SS. In addition, the
433 RD is always less than 10 % when estimating N_{CCN} using the mean value of κ_{chem} ,
434 suggesting that $\kappa = 0.31$ is a good proxy for chemical composition when estimating
435 N_{CCN} at XT.

436 In summary, particle size is the most important factor influencing the aerosol
437 activation ability at XT, especially at larger SS levels. The mixing state and chemical
438 composition were not as important when estimating N_{CCN} because the particles were
439 highly aged and internally mixed at XT during the field experiment, and aerosol
440 hygroscopicity was not sensitive to estimates of N_{CCN} .

441 5. Summary and conclusions

442 The Atmosphere-Aerosol-Boundary Layer-Cloud (A²BC) Interaction Joint
443 Experiment was carried out at a polluted site located in the central North China Plain



444 (NCP) from 1 May to 15 June of 2016. The aerosol hygroscopicity, mixing state and
445 CCN activity at the site Xingtai (XT) were investigated in this study.

446 In general, the probability density function of the hygroscopicity parameter
447 (κ -PDF) for 40–200 nm particles is a unimodal distribution, which is different from
448 distributions at other sites in China. Particles of all sizes cover a large range of κ_{gf}
449 (mostly from 0 to 0.8) and show similar κ -PDF patterns, suggesting that the
450 hygroscopic compounds in these particles from 40 nm to 200 nm were similar at XT.
451 The κ -PDF patterns also suggests that the particles were highly aged and internally
452 mixed at XT during the field experiment. This is likely related to strong
453 photochemical reactions.

454 The mean κ_{gf} for different particle sizes are larger in the daytime than at night.
455 Daytime and nighttime κ_{gf} differences decrease with increasing particle size. This
456 illustrates that the impact of photochemical reactions on aerosol hygroscopicity was
457 strong and that the effect became weaker as particle sizes increased. The enhanced
458 hygroscopicity of 40–200 nm particles was likely caused by the coating of sulfates or
459 secondary organics while the effect was more significant for 40 nm particles.
460 Compared with other sites in China, the aerosol hygroscopicity was much larger at XT
461 because of the strong photochemical reactions and the sufficient precursors. The
462 comparison also shows that the hygroscopicity of particles from different emissions
463 and chemical processes differed.

464 New particle formation events occurred frequently at XT during the field
465 experiment. The evolution of the planetary boundary layer (PBL) played a dominant



466 role on the aerosol mass concentration, while particle formation and growth had a
467 greater influence on the variation in the aerosol number concentration. Particle size
468 was the most important factor influencing the aerosol activation ability and the CCN
469 number concentration at XT during the field experiment, especially at larger
470 supersaturations (SS). Although the estimated N_{CCN} correlated well with
471 measurements ($R^2 \geq 0.85$), N_{CCN} was overestimated because of measurement
472 uncertainties. The effect of chemical composition on N_{CCN} was weaker relative to the
473 particle size. Sensitivity tests show that the impact of chemical composition on N_{CCN}
474 became weaker as SS increased, suggesting that the effect of chemical composition on
475 N_{CCN} estimates is less important at larger SS. The value $\kappa = 0.31$ is a good proxy for
476 chemical composition when estimating N_{CCN} for the model at XT.

477 Our results show that aerosol properties in the middle of the NCP differ from
478 those in the northern part of the NCP and other regions in China. This is because there
479 are more industrial emissions in the central NCP. The plentitude of gas precursors and
480 strong photochemical reactions at XT make aerosol properties there different from
481 those at sites under other polluted conditions. More field measurements on
482 gas-particle transformation and aerosol properties in this region are needed, which
483 would be meaningful for studying the haze formation mechanism and climate change
484 in the NCP.

485
486 *Data availability.* The data used in the study are available from the first author upon
487 request (wang.yuying@mail.bnu.edu.cn).

488
489 *Competing interests.* The authors declare that they have no conflict of interest.
490



491 *Author contribution.* Z.L. and Y.W. designed the experiment, Y.W., Y.Z., and W.D.
492 carried it out and analyzed the data, other co-authors participated in science discussions
493 and suggested analyses. Y.W. prepared the manuscript with contributions from all
494 co-authors.

495
496 *Acknowledgements.* This work was funded by the National Natural Science
497 Foundation of China (NSFC) research projects (grant no. 91544217, 41675141), the
498 National Basic Research Program of China “973” (grant no. 2013CB955801), and the
499 China Scholarship Council (award no. 201706040194). We also thank all participants
500 in the field campaign for their tireless work and cooperation.

501 **References**

- 502 Albrecht B.A.: Aerosols, Cloud Microphysics, and Fractional Cloudiness, *Science*, 245, 1227-30, 1989.
503 Brooks I.M.: Finding boundary layer top: Application of a wavelet covariance transform to lidar
504 backscatter profiles, *J. Atmos. Ocean. Tech.*, 20, 1092-1105, 2003.
- 505 Chu Y., Sauerwein M. and Chan C.K.: Hygroscopic and phase transition properties of alkyl aminium
506 sulfates at low relative humidities, *Phys. Chem. Chem. Phys.*, 17, 19789-19796,
507 <https://doi.org/10.1039/c5cp02404h>, 2015.
- 508 Cohn S.A. and Angevine W.M.: Boundary layer height and entrainment zone thickness measured by
509 lidars and wind-profiling radars, *Journal of Applied Meteorology*, 39, 1233-1247, 2000.
- 510 Covert D.S., Charlson R.J. and Ahlquist N.C.: A study of the relationship of chemical composition and
511 humidity to light scattering by aerosols, *Journal of Applied Meteorology*, 11, 968-976, 1972.
- 512 Cruz C.N. and Pandis S.N.: Deliquescence and hygroscopic growth of mixed inorganic-organic
513 atmospheric aerosol, *Environ. Sci. Technol.*, 34, 4313-4319, <https://doi.org/10.1021/es9907109>,
514 2000.
- 515 Cubison M.J., Ervens B., Feingold G., Docherty K.S., Ulbrich I.M., Shields L., Prather K., Hering S.
516 and Jimenez J.L.: The influence of chemical composition and mixing state of Los Angeles urban
517 aerosol on CCN number and cloud properties, *Atmos. Chem. Phys.*, 8, 5649-5667,
518 <https://doi.org/10.5194/acp-8-5649-2008>, 2008.
- 519 Daniel R., Ulrike L., Raga G.B., O'Dowd C.D., Markku K., Sandro F., Anni R. and Andreae M.O.:
520 Flood or drought: how do aerosols affect precipitation?, *Science*, 321, 1309-1313,
521 <https://doi.org/10.1126/science.1160606>, 2008.
- 522 Deng Z.Z., Ma N., Liu P.F., Xu W.Y., Zhao C.S., Ran L., Chen J., Liang Z., Liang S. and Huang M.Y.:
523 Size-resolved and bulk activation properties of aerosols in the North China Plain, *Atmos. Chem.*
524 *Phys.*, 11, 3835-3846, <https://doi.org/10.5194/acp-11-3835-2011>, 2011.
- 525 Eichler H., Cheng Y.F., Birmili W., Nowak A., Wiedensohler A., Brüggemann E., Gnauk T.,
526 Herrmann H., Althausen D. and Ansmann A.: Hygroscopic properties and extinction of aerosol
527 particles at ambient relative humidity in South-Eastern China, *Atmos Environ*, 42, 6321-6334,
528 <https://doi.org/10.1016/j.atmosenv.2008.05.007>, 2008.
- 529 Ervens B., Cubison M., Andrews E., Feingold G., Ogren J.A., Jimenez J.L., DeCarlo P. and Nenes A.:
530 Prediction of cloud condensation nucleus number concentration using measurements of aerosol size
531 distributions and composition and light scattering enhancement due to humidity, *J. Geophys.*
532 *Res.-Atmos.*, 112, <https://doi.org/10.1029/2006JD007426>, 2007.
- 533 Fu G.Q., Xu W.Y., Yang R.F., Li J.B. and Zhao C.S.: The distribution and trends of fog and haze in the



- 534 North China Plain over the past 30 years, *Atmos. Chem. Phys.*, 14, 11949-11958,
535 <https://doi.org/10.5194/acp-14-11949-2014>, 2014.
- 536 Gomez-Hernandez M., McKeown M., Secrest J., Marrero-Ortiz W., Lavi A., Rudich Y., Collins D.R.
537 and Zhang R.: Hygroscopic Characteristics of Alkylaluminium Carboxylate Aerosols, *Environ. Sci.*
538 *Technol.*, 50, 2292-2300, <https://dx.doi.org/10.1021/acs.est.5b04691>, 2016.
- 539 Guo S., Hu M., Lin Y., Gomez-Hernandez M., Zamora M.L., Peng J., Collins D.R. and Zhang R.:
540 OH-Initiated Oxidation of m-Xylene on Black Carbon Aging, *Environ. Sci. Technol.*, 50, 8605-8612,
541 <https://dx.doi.org/10.1021/acs.est.6b01272>, 2016.
- 542 Gysel M., Crosier J., Topping D.O., Whitehead J.D., Bower K.N., Cubison M.J., Williams P.I., Flynn
543 M.J., McFiggans G.B. and Coe H.: Closure study between chemical composition and hygroscopic
544 growth of aerosol particles during TORCH2, *Atmos. Chem. Phys.*, 7, 6131-6144,
545 <https://doi.org/10.5194/acp-7-6131-2007>, 2007.
- 546 Huang R., Zhang Y., Bozzetti C., Ho K., Cao J., Han Y., Daellenbach K.R., Slowik J.G., Platt S.M.,
547 Canonaco F., Zotter P., Wolf R., Pieber S.M., Bruns E.A., Crippa M., Ciarelli G., Piazzalunga A.,
548 Schwikowski M., Abbaszade G., Schnelle-Kreis J., Zimmermann R., An Z., Szidat S., Baltensperger
549 U., Haddad I.E. and Prévôt A.S.H.: High secondary aerosol contribution to particulate pollution
550 during haze events in China, *Nature*, <https://doi.org/10.1038/nature13774>, 2014.
- 551 IPCC: Climate change 2013: Scientific basis, Fifth assessment of the Inter-governmental Panel on
552 Climate Change, Cambridge University Press, 2013.
- 553 Jacobson M.C., Hansson H.C., Noone K.J. and Charlson R.J.: Organic atmospheric aerosols: Review
554 and state of the science, *Rev. Geophys.*, 38, 267-294, <https://doi.org/10.1029/1998RG000045>, 2000.
- 555 Jiang R.X., Tan H.B., Tang L.L., Cai M.F., Yin Y., Li F., Liu L., Xu H.B., Chan P.W., Deng X.J. and
556 Wu D.: Comparison of aerosol hygroscopicity and mixing state between winter and summer seasons
557 in Pearl River Delta region, China, *Atmos. Res.*, 169, 160-170,
558 <https://doi.org/10.1016/j.atmosres.2015.09.031>, 2016.
- 559 Jimenez J.L., Canagaratna M.R., Donahue N.M., Prevot A., Zhang Q., Kroll J.H., DeCarlo P.F., Allan
560 J.D., Coe H. and Ng N.L.: Evolution of organic aerosols in the atmosphere, *Science*, 326, 1525-1529,
561 <https://doi.org/10.1126/science.1180353>, 2009.
- 562 Juranyi Z., Gysel M., Weingartner E., DeCarlo P.F., Kammermann L. and Baltensperger U.: Measured
563 and modelled cloud condensation nuclei number concentration at the high alpine site Jungfraujoch,
564 *Atmos. Chem. Phys.*, 10, 7891-7906, <https://doi.org/10.5194/acp-10-7891-2010>, 2010.
- 565 Köhler H.: The nucleus in and the growth of hygroscopic droplets, *Transactions of the Faraday Society*,
566 32, 1152-1161, 1936.
- 567 Kulmala M., Petäjä T., Nieminen T., Sipilä M., Manninen H.E., Lehtipalo K., Dal Maso M., Aalto P.P.,
568 Junninen H. and Paasonen P.: Measurement of the nucleation of atmospheric aerosol particles, *Nat.*
569 *Protoc.*, 7, 1651-1667, <https://doi.org/10.1038/nprot.2012.091>, 2012.
- 570 Lance S., Nenes A., Medina J. and Smith J.N.: Mapping the operation of the DMT continuous flow
571 CCN counter, *Aerosol Sci. Tech.*, 40, 242-254, <http://dx.doi.org/10.1080/02786820500543290>,
572 2006.
- 573 Lebo Z.J., Shipway B.J., Fan J., Geresdi I., Hill A., Miltenberger A., Morrison H., Rosenberg P.,
574 Varble A. and Xue L.: Challenges for cloud modeling in the context of aerosol-cloud-precipitation
575 interactions, *B. Am. Meteorol. Soc.*, <https://doi.org/10.1175/BAMS-D-16-0291.1>, 2017.
- 576 Li Y., Zhang F., Li Z., Sun L., Wang Z., Li P., Sun Y., Ren J., Wang Y. and Cribb M.: Influences of
577 aerosol physiochemical properties and new particle formation on CCN activity from observation at a



- 578 suburban site of China, *Atmos. Res.*, 188, 80-89, <https://doi.org/10.1016/j.atmosres.2017.01.009>,
579 2017.
- 580 Li Z., Lau W.M., Ramanathan V., Wu G., Ding Y., Manoj M.G., Liu J., Qian Y., Li J. and Zhou T.:
581 Aerosol and monsoon climate interactions over Asia, *Rev. Geophys.*,
582 <https://doi.org/10.1002/2015RG000500>, 2016.
- 583 Li Z., Daniel R. and Fan J.W.: Aerosols and Their Impact on Radiation, Clouds, Precipitation, and
584 Severe Weather Events, *Oxford Research Encyclopedias: Environmental science*,
585 <https://doi.org/10.1093/acrefore/9780199389414.013.126>, 2017.
- 586 Liu P.F., Zhao C.S., Bel T.G., Hallbauer E., Nowak A., Ran L., Xu W.Y., Deng Z.Z., Ma N.,
587 Mildenerger K., Henning S., Stratmann F. and Wiedensohler A.: Hygroscopic properties of aerosol
588 particles at high relative humidity and their diurnal variations in the North China Plain, *Atmos.*
589 *Chem. Phys.*, <https://doi.org/10.5194/acp-11-3479-2011>, 2011.
- 590 Lopez-Yglesias X.F., Yeung M.C., Dey S.E., Brechtel F.J. and Chan C.K.: Performance Evaluation of
591 the Brechtel Mfg. Humidified Tandem Differential Mobility Analyzer (BMI HTDMA) for Studying
592 Hygroscopic Properties of Aerosol Particles, *Aerosol Sci Tech*, 48, 969-980,
593 <http://dx.doi.org/10.1080/02786826.2014.952366>, 2014.
- 594 Meng J.W., Yeung M.C., Li Y.J., Lee B.Y.L. and Chan C.K.: Size-resolved cloud condensation nuclei
595 (CCN) activity and closure analysis at the HKUST Supersite in Hong Kong, *Atmos. Chem. Phys.*, 14,
596 10267-10282, <https://doi.org/10.5194/acp-14-10267-2014>, 2014.
- 597 Ng N.L., Herndon S.C., Trimborn A., Canagaratna M.R., Croteau P.L., Onasch T.B., Sueper D.,
598 Worsnop D.R., Zhang Q. and Sun Y.L.: An Aerosol Chemical Speciation Monitor (ACSM) for
599 routine monitoring of the composition and mass concentrations of ambient aerosol, *Aerosol Sci.*
600 *Tech.*, 45, 780-794, <http://dx.doi.org/10.1080/02786826.2011.560211>, 2011.
- 601 Peng J., Hu M., Guo S., Du Z., Zheng J., Shang D., Zamora M.L., Zeng L., Shao M. and Wu Y.:
602 Markedly enhanced absorption and direct radiative forcing of black carbon under polluted urban
603 environments, *Proceedings of the National Academy of Sciences*, 113, 4266-4271,
604 <https://doi.org/10.1073/pnas.1602310113>, 2016.
- 605 Petters M.D. and Kreidenweis S.M.: A single parameter representation of hygroscopic growth and
606 cloud condensation nucleus activity, *Atmos. Chem. Phys.*, 7, 1961-1971,
607 <https://doi.org/10.5194/acp-7-1961-2007>, 2007.
- 608 Qiu C. and Zhang R.: Physicochemical Properties of Alkylammonium Sulfates: Hygroscopicity,
609 Thermostability, and Density, *Environ. Sci. Technol.*, 46, 4474-4480,
610 <https://dx.doi.org/10.1021/es3004377>, 2012.
- 611 Quan J., Gao Y., Zhang Q., Tie X., Cao J., Han S., Meng J., Chen P. and Zhao D.: Evolution of
612 planetary boundary layer under different weather conditions, and its impact on aerosol
613 concentrations, *Particuology*, 11, 34-40, <https://doi.org/10.1016/j.partic.2012.04.005>, 2013.
- 614 Ramanathan V., Crutzen P.J., Kiehl J.T. and Rosenfeld D.: Aerosols, climate, and the hydrological
615 cycle, *Science*, 294, 2119-2124, <https://doi.org/10.1126/science.1064034>, 2001.
- 616 Rose D., Gunthe S.S., Mikhailov E., Frank G.P., Dusek U., Andreae M.O. and Pöschl U.: Calibration
617 and measurement uncertainties of a continuous-flow cloud condensation nuclei counter
618 (DMT-CCNC): CCN activation of ammonium sulfate and sodium chloride aerosol particles in theory
619 and experiment, *Atmos. Chem. Phys.*, 8, 1153-1179, <https://doi.org/10.5194/acp-8-1153-2008>, 2008.
- 620 Stock M., Cheng Y.F., Birmili W., Massling A., Wehner B., Müller T., Leinert S., Kalivitis N.,
621 Mihalopoulos N. and Wiedensohler A.: Hygroscopic properties of atmospheric aerosol particles over



- 622 the Eastern Mediterranean: implications for regional direct radiative forcing under clean and polluted
623 conditions, *Atmos. Chem. Phys.*, 11, 4251-4271, <https://doi.org/10.5194/acp-11-4251-2011>, 2011.
- 624 Stokes R.H. and Robinson R.A.: Interactions in aqueous nonelectrolyte solutions. I. Solute-solvent
625 equilibria, *The Journal of Physical Chemistry*, 70, 2126-2131, 1966.
- 626 Stolzenburg M.R. and McMurry P.H.: Equations governing single and tandem DMA configurations
627 and a new lognormal approximation to the transfer function, *Aerosol Sci. Tech.*, 42, 421-432,
628 <http://dx.doi.org/10.1080/02786820802157823>, 2008.
- 629 Stolzenburg M.R. and McMurry P.H.: TDMAFIT user's manual, University of Minnesota, Department
630 of Mechanical Engineering, Particle Technology Laboratory, Minneapolis, 1-61, 1988.
- 631 Sun Y., Wang Z., Dong H., Yang T., Li J., Pan X., Chen P. and Jayne J.T.: Characterization of summer
632 organic and inorganic aerosols in Beijing, China with an Aerosol Chemical Speciation Monitor,
633 *Atmos. Environ.*, 51, 250-259, <https://doi.org/10.1016/j.atmosenv.2012.01.013>, 2012.
- 634 Swietlicki E., Hansson H.C., HÄMeri K., Svenningsson B., Massling A., McFiggans G., McMurry
635 P.H., PetÄJÄ T., Tunved P., Gysel M., Topping D., Weingartner E., Baltensperger U., Rissler J.,
636 Wiedensohler A. and Kulmala M.: Hygroscopic properties of submicrometer atmospheric aerosol
637 particles measured with H-TDMA instruments in various environments—a review, *Tellus B*, 60,
638 432-469, <https://doi.org/10.1111/j.1600-0889.2008.00350.x>, 2008.
- 639 Tan H., Xu H., Wan Q., Li F., Deng X., Chan P.W., Xia D. and Yin Y.: Design and application of an
640 unattended multifunctional H-TDMA system, *J. Atmos. Ocean. Tech.*, 30, 1136-1148,
641 <https://doi.org/10.1175/JTECH-D-12-00129.1>, 2013.
- 642 Tritscher T., Juranyi Z., Martin M., Chirico R., Gysel M., Heringa M.F., DeCarlo P.F., Sierau B.,
643 Prevot A.S.H., Weingartner E. and Baltensperger U.: Changes of hygroscopicity and morphology
644 during ageing of diesel soot, *Environ. Res. Lett.*, 6, <https://doi.org/10.1088/1748-9326/6/3/034026>,
645 2011.
- 646 Twomey S.: Pollution and the planetary albedo, *Atmos. Environ.*, 8, 1251-1256, 1974.
- 647 Ulbrich I.M., Canagaratna M.R., Zhang Q., Worsnop D.R. and Jimenez J.L.: Interpretation of organic
648 components from Positive Matrix Factorization of aerosol mass spectrometric data, *Atmos. Chem.*
649 *Phys.*, 9, 2891-2918, <https://doi.org/10.5194/acp-9-2891-2009>, 2009.
- 650 Wang L.T., Wei Z., Yang J., Zhang Y., Zhang F.F., Su J., Meng C.C. and Zhang Q.: The 2013 severe
651 haze over southern Hebei, China: model evaluation, source apportionment, and policy implications,
652 *Atmos. Chem. Phys.*, 14, 3151-3173, <https://doi.org/10.5194/acp-14-3151-2014>, 2014.
- 653 Wang Y., Zhang F., Li Z., Tan H., Xu H., Ren J., Zhao J., Du W. and Sun Y.: Enhanced
654 hydrophobicity and volatility of submicron aerosols under severe emission control conditions in
655 Beijing, *Atmos. Chem. Phys.*, 17, 5239-5251, <https://doi.org/10.5194/acp-17-5239-2017>, 2017.
- 656 Wang Z., Wu Z., Yue D., Shang D., Guo S., Sun J., Ding A., Wang L., Jiang J. and Guo H.: New
657 particle formation in China: Current knowledge and further directions, *Sci. Total Environ.*, 577,
658 258-266, <https://doi.org/10.1016/j.scitotenv.2016.10.177>, 2017.
- 659 Wu Z.J., Zheng J., Shang D.J., Du Z.F., Wu Y.S., Zeng L.M., Wiedensohler A. and Hu M.: Particle
660 hygroscopicity and its link to chemical composition in the urban atmosphere of Beijing, China,
661 during summertime, *Atmos. Chem. Phys.*, 16, 1123-1138, <https://doi.org/10.5194/acp-16-1123-2016>,
662 2016.
- 663 Ye X., Tang C., Yin Z., Chen J., Ma Z., Kong L., Yang X., Gao W. and Geng F.: Hygroscopic growth
664 of urban aerosol particles during the 2009 Mirage-Shanghai Campaign, *Atmos. Environ.*, 64,
665 263-269, <https://doi.org/10.1016/j.atmosenv.2012.09.064>, 2013.



666 Zhang F., Li Y., Li Z., Sun L., Li R., Zhao C., Wang P., Sun Y., Liu X., Li J., Li P., Ren G. and Fan T.:
 667 Aerosol hygroscopicity and cloud condensation nuclei activity during the AC³Exp campaign:
 668 implications for cloud condensation nuclei parameterization, *Atmos. Chem. Phys.*, 14, 13423-13437,
 669 <https://doi.org/10.5194/acp-14-13423-2014>, 2014.

670 Zhang F., Li Z., Li Y., Sun Y., Wang Z., Li P., Sun L., Wang P., Cribb M., Zhao C., Fan T., Yang X.
 671 and Wang Q.: Impacts of organic aerosols and its oxidation level on CCN activity from measurement
 672 at a suburban site in China, *Atmos. Chem. Phys.*, 16, 5413-5425,
 673 <https://doi.org/10.5194/acp-16-5413-2016>, 2016.

674 Zhang R., Khalizov A.F., Pagels J., Zhang D., Xue H. and McMurry P.H.: Variability in morphology,
 675 hygroscopicity, and optical properties of soot aerosols during atmospheric processing, *Proceedings*
 676 *of the National Academy of Sciences*, 105, 10291-10296,
 677 <https://doi.org/10.1073/pnas.0804860105>, 2008.

678 Zhang R., Wang L., Khalizov A.F., Zhao J., Zheng J., McGraw R.L. and Molina L.T.: Formation of
 679 nanoparticles of blue haze enhanced by anthropogenic pollution, *Proceedings of the National*
 680 *Academy of Sciences*, 106, 17650-17654, <https://doi.org/10.1073/pnas.0910125106>, 2009.

681 Zhang S.L., Ma N., Kecorius S., Wang P.C., Hu M., Wang Z.B., Größ J., Wu Z.J. and Wiedensohler A.:
 682 Mixing state of atmospheric particles over the North China Plain, *Atmos. Environ.*, 125, Part A,
 683 152-164, <https://doi.org/10.1016/j.atmosenv.2015.10.053>, 2016.

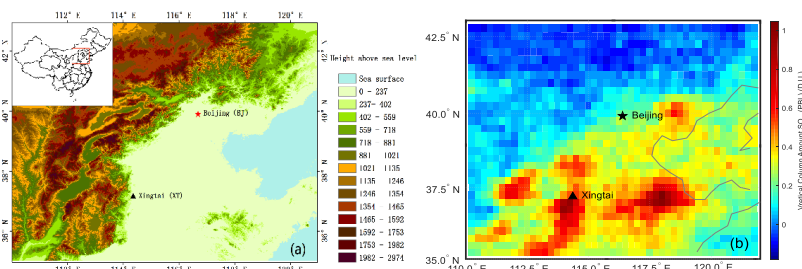
684 Zhu Y., Zhang J., Wang J., Chen W., Han Y., Ye C., Li Y., Liu J., Zeng L., Wu Y., Wang X., Wang W.,
 685 Chen J. and Zhu T.: Distribution and sources of air pollutants in the North China Plain based on
 686 on-road mobile measurements, *Atmos. Chem. Phys.*, 16, 12551-12565,
 687 <https://doi.org/10.5194/acp-16-12551-2016>, 2016.

688
 689
 690
 691
 692

Table 1. The number fractions of different hygroscopic groups for different particle sizes.

	40 nm	80 nm	110 nm	150 nm	200 nm
NH	5.1 %	5.0 %	5.1 %	5.0 %	5.7 %
LH	4.8 %	4.2 %	4.3 %	4.7 %	5.1 %
MH	90.1 %	90.8 %	90.6 %	90.3 %	89.2 %

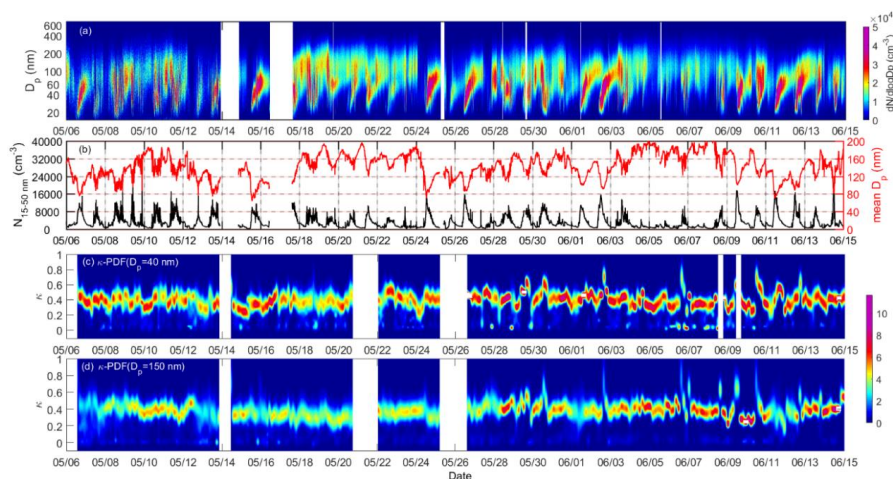
693
 694
 695



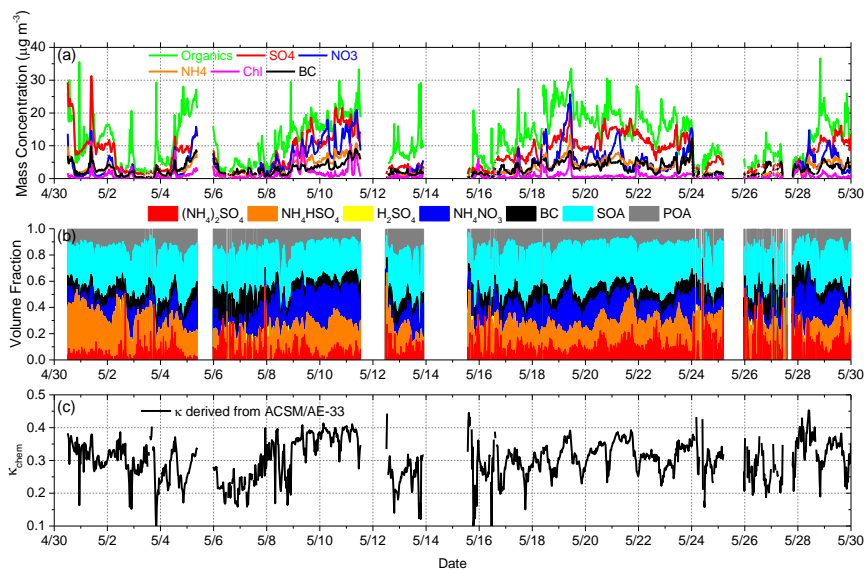
696



697 **Figure 1.** (a) Map showing the locations of the sampling sites and (b) the distribution
698 of mean SO_2 concentrations from May of 2012 to 2016.
699



700
701 **Figure 2.** The time series of (a) particle number size distribution (PNSD), (b) aerosol
702 number concentration in the 15–50 nm range ($N_{15-50 \text{ nm}}$) and the mean diameter (D_p),
703 (c) the probability density function of κ_{gf} (κ -PDF) for 40 nm and (d) 150 nm
704 particles from 6 May to 15 June of 2016.
705
706



707

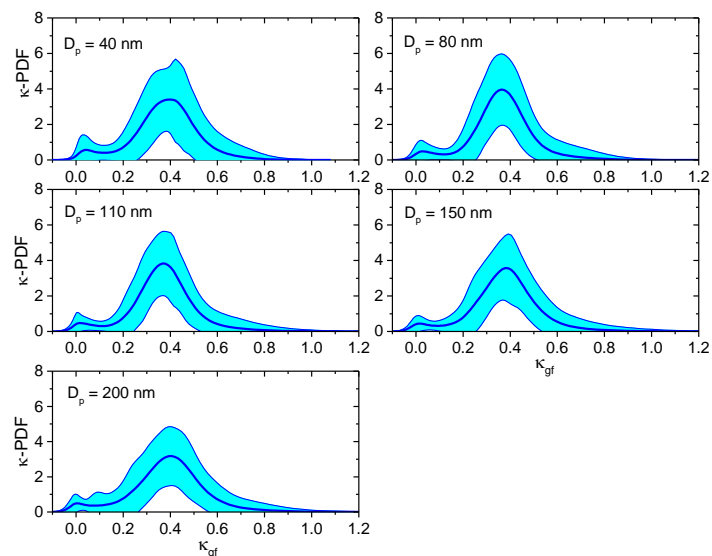
708 **Figure 3.** Time series of (a) the bulk mass concentration of aerosol species in PM_{10} , (b)

709 the volume fractions of POA, SOA, BC, and inorganics with the simplified ion

710 pairing scheme, and (c) the hygroscopicity parameter derived from the chemical

711 compositions (κ_{chem}).

712



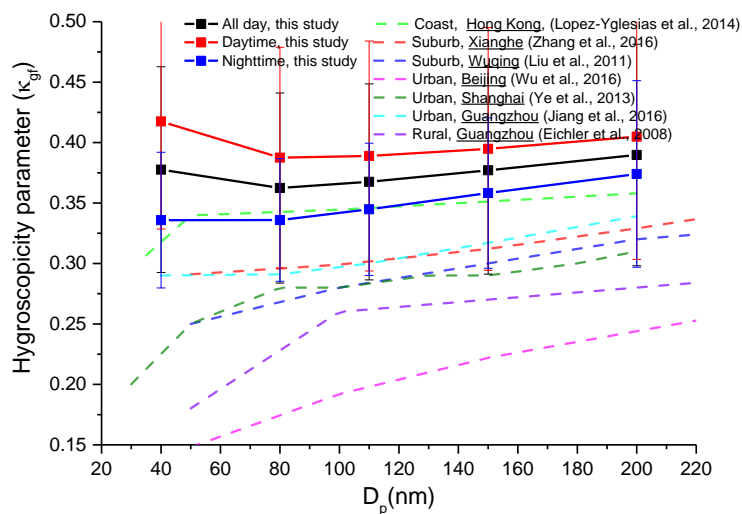
713

714 **Figure 4.** Mean probability density functions of κ_{gf} (κ -PDF) for different particle

715 sizes and their standard deviations (shaded areas) derived from H-TDMA data and

716 measured at RH = 85 %.

717

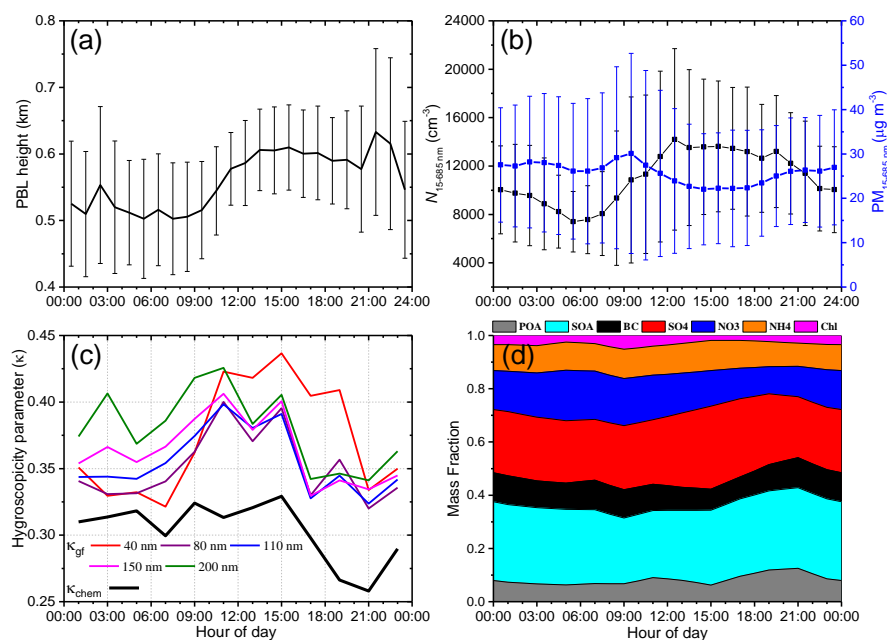


718

719 **Figure 5.** Size-resolved aerosol hygroscopicity parameter (κ_{gf}) derived from

720 H-TDMA data at XT and at other sites in China.

721



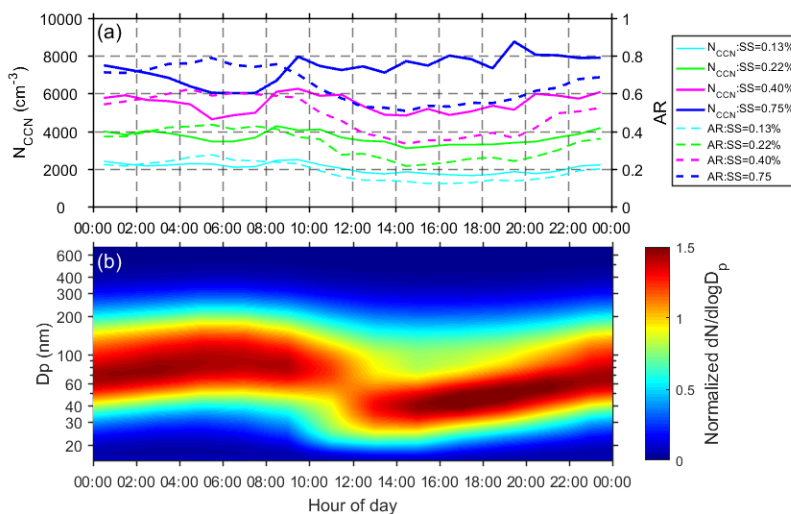
722

723

724

Figure 6. Diurnal variations in (a) planetary boundary layer (PBL) height retrieved
725 from the MPL, (b) aerosol number and mass concentrations in the 15–685 nm range
726 ($N_{15-685\text{ nm}}$ and $\text{PM}_{15-685\text{ nm}}$, respectively) derived from the SMPS (an aerosol density
727 of 1.6 g cm^{-3} is assumed), (c) the hygroscopicity parameter derived from the
728 hygroscopic growth factor (κ_{gf}) and predicted from the bulk chemical composition
729 (κ_{chem}), and (d) the mass fractions of different species.

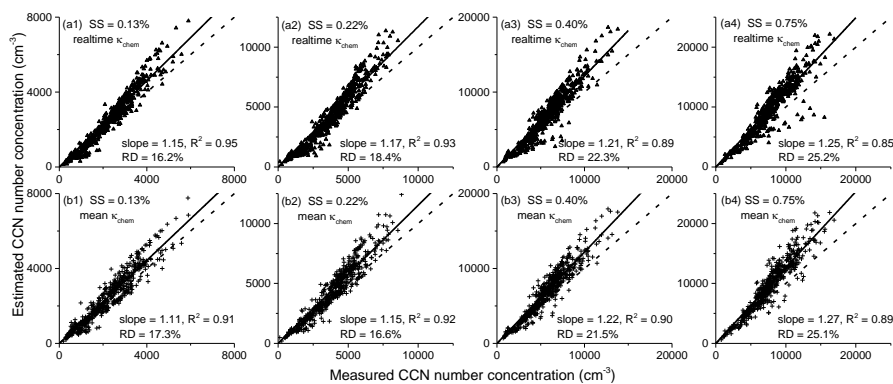
730



731

732 **Figure 7.** Diurnal variations in (a) CCN number concentration (N_{CCN}) and activation
 733 ratio (AR), and (b) the normalized aerosol size distribution in the 15–685 nm particle
 734 size range.

735



736

737

738 **Figure 8.** Estimated versus measured CCN number concentration for ambient
 739 aerosols at four different supersaturation levels. The N_{CCN} is estimated based on
 740 κ -Köhler theory, using the real-time κ_{chem} (a1-a4) and the mean κ_{chem} (b1-b4).
 741 The slope and correlation coefficient (R^2) of the linear regression, and the relative



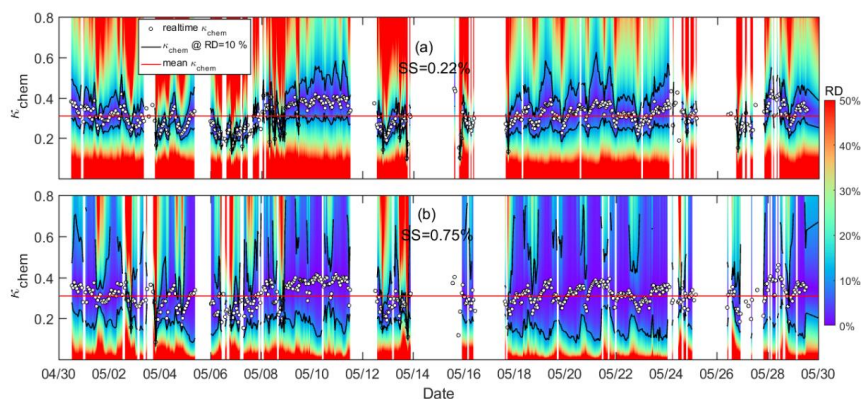
742 deviation of estimated N_{CCN} ($RD = |N_{CCN_estimated} - N_{CCN_measured}| / N_{CCN_measured}$) are

743 shown in each panel. The regression line is overlaid on the measurements (solid line)

744 and the dashed line is the 1:1 line.

745

746



747

748 **Figure 9.** Sensitivity of N_{CCN} estimates to κ_{chem} as a function of time at (a) $SS =$

749 0.22% and (b) $SS = 0.75\%$. The color scale indicates the relative deviation (RD) of

750 the CCN estimates using the κ_{chem} value shown on the ordinate. In each panel, open

751 circles show the real-time κ_{chem} . Note that RD is by definition zero at these points.

752 The black line is κ at $RD = 10\%$ and the red line is the mean value for κ_{chem} (0.31).

753 Figure S6 in the supplement shows the same plots but for $SS = 0.13\%$ and 0.40% .

754